Title
CO2 Electrolysis Using Metal-Supported Solid Oxide Cells with Infiltrated Pr0.5Sr0.4Mn0.2Fe0.8O3-δ Catalyst

Authors
Hu, Boxun
Park, Ka-Young
Sarycheva, Asia
et al.

Publication Date
2025-01-14

DOI
10.1149/1945-7111/adaa23

CO_2 Electrolysis using Metal-Supported Solid Oxide Cells with Infiltrated $Pr_{0.5}Sr_{0.4}Mn_{0.2}Fe_{0.8}O_{3-\delta}$ Catalyst

Boxun Hu[a], Ka-Young Park[b], Asia Sarycheva[a], and Robert Kostecki[a], Fanglin Chen[b], and Michael C. Tucker[a,*]

[a] Energy Storage and Distributed Resources, Lawrence Berkeley National Laboratory, Berkeley, CA 94720, USA

[b] Department of Mechanical Engineering, University of South Carolina, Columbia, SC 29208, USA

*Corresponding author: mctucker@lbl.gov

Abstract

Electrochemical conversion of CO_2 to CO is demonstrated with symmetric-structured metal supported solid oxide cells (MS-SOC). Perovskite $Pr_{0.5}Sr_{0.4}Mn_{0.2}Fe_{0.8}O_{3-\delta}$ (PSMF) and Pr_6O_{11} catalysts were infiltrated into the MS-SOC cathode and anode, using 3 cycles with firing at 850°C and 8 cycles with firing at 800°C, respectively. Upon reduction during operation, the perovskite PSMF was transformed to Ruddlesden–Popper structure with a highly efficient electrocatalytic activity. The impact of operating temperature (600-800°C) and overpotential (0-1.8 V) on the CO_2 conversion was investigated. The highest CO_2 conversion of 57.2% was achieved at 750°C and 1.8 V. During extended operation for 150 h at 750°C and 1.2V, a cell demonstrated relatively stable performance, with initial current density of 535 mA cm^{-2} and CO_2 conversion of 23%. Degradation mechanisms were studied by posttest characterization.

Key words: CO_2 electrolysis, carbon monoxide, $Pr_{0.5}Sr_{0.4}Mn_{0.2}Fe_{0.8}O_{3-\delta}$, *in situ* exsolution, infiltration, metal-supported solid oxide cell

1. Introduction

Electrochemical conversion of CO_2 to CO and O_2 using solid oxide electrolyzers (SOE) is useful for many applications including space exploration, chemical synthesis, and energy storage (1). The Mars Oxygen ISRU Experiment (MOXIE) converted carbon dioxide in the Mars atmosphere using a SOE stack to produce high-purity oxygen and CO, with a vision for life support and ascent vehicle propellant oxidant during human expeditions on Mars (2). Oxygen ions extracted from CO_2 were utilized for electrochemical oxidative coupling of methane to synthesize ethylene with C2 selectivity of 75.6% at 850°C (3). CO_2 conversion provides a simple approach to simultaneously mitigate greenhouse emission and store surplus energy, which reduces electricity network variation due to increased intermittent renewable energy (such as solar and wind) utilization (4). CO is a feedstock or intermediate for the production of methanol and hydrocarbon fuels via the Fischer-Tropsch synthesis (5, 6). Power-to-fuel systems based on SOEs are highly suitable for accelerating application of intermittent renewable energy (7), and synthesis of carbon-neutral fuels and chemicals production have been suggested based on economic analyses (8). A relatively high operating temperature range of 600 to 750°C promotes energy efficiency and allows integration of heat. High temperature electrolysis in SOEs has advantages of high efficiency, proven durability, and operation at commercially relevant current densities (>0.5 A cm^{-2}) (9-11).

Selection of a proper CO_2 reduction catalyst is critical to achieve efficient and durable CO_2 electrolysis (11). Metal-oxide cathode catalysts, including Ni-YSZ, Ni-CeO_2, Nb-MnO_2, and supported bi-alloy-oxide catalysts have been studied (12), however, carbon deposition and catalyst particle agglomeration reduce the triple phase boundary (TPB) and degrade the cathode performance (13, 14). Mixed conductive perovskite catalysts ((La,Sr) (Cr,Mn, Fe,Ni)O_3 (15-17),

doped (La,Sr)TiO_3 (18, 19), and Sr(Fe,Mn,Mo)O_3 (20, 21), have been selected due to their redox stability and coking resistance. However, these perovskite catalysts showed limited electronic conductivity and catalytic activity compared to conventional metal-oxide catalysts. To overcome this limitation, *in situ* exsolution of metallic particles on perovskite catalysts improved catalytic activity and stability for CO_2 electrolysis (22-25). Recently, $La_{0.8}Sr_{0.2}Ga_{0.8}Mg_{0.2}O_{3-\delta}$ (LSGM)-electrolyte supported SOCs with Ruddlesden–Popper structured $Pr_{1.2}Sr_{0.8}Mn_{0.4}Fe_{0.6}O_{4-\delta}$ (RP-PSMF) with *in situ* Fe nanoparticles exsolved at 800°C in H_2 as CO_2 electrode achieved a high current density of 1.61 A cm^{-2} at 750°C and no degradation was observed during 100 h operation (11). Here, this catalyst composition is adapted for use in metal-supported cells. More information about RP oxides and *in situ* nanoparticle exsolution can be found in a recent review (26).

Metal supported solid oxide cells with symmetric structure (MS-SOCs) developed at Lawrence Berkeley National Laboratory have advantages of rapid start-up, mechanical ruggedness, redox tolerance, dynamic operation, and low-cost materials (27-32). The co-sintered stainless steel and zirconia structure is an ideal platform for various types of electrochemical devices, which can be prepared by infiltrating a wide variety of electrocatalysts into the structure (Fig. 1a). The infiltration technique is a simple, low-cost and effective method for loading high surface area catalyst in the pores of electrodes at a relative low temperature (400-850°C), thereby avoiding catalyst decomposition or reaction between the metal support and catalysts that would be expected in the case of co-sintering the metal and catalysts at higher temperature. The metal-supported zirconia platform has been infiltrated with various catalysts to produce cells for: fuel cell operation with hydrogen, ethanol, and natural gas (33-35); electrolysis of steam to produce hydrogen (36); and, oxidative coupling of methane to synthesize ethylene (37).

In this study a metal supported $Pr_{0.5}Sr_{0.4}Mn_{0.2}Fe_{0.8}O_{3-\delta}$ (PSMF)-ScSZ‖ScSZ‖Pr_6O_{11}-ScSZ cell has been developed for direct CO_2 reduction electrolysis. Pr_6O_{11} was selected as oxygen electrode catalyst due to its proven activity for oxygen evolution and reduction reactions (31, 37, 38). Optimal catalyst infiltration processing and operating conditions for infiltrated PSMF are developed here.

2. Experimental Methods

2.1. Cell Structure Fabrication

The cell fabrication processes were adapted from previous procedures, with the stainless steel and ceramic cell structure unchanged, and the infiltration process modified for PSMF deposition (31, 37) (Fig 1). One-inch diameter symmetrical metal-supported button cells were fabricated using P434L stainless steel powder (Ametek, USA) and 10Sc1Ce-doped zirconia (ScSZ, Daiichi Kigenso Kagaku Kogyo) powder via tape casting, lamination, laser cutting, debinding, and sintering at 1350°C for 2 h in 2% H_2 to obtain dense electrolyte and porous electrodes. Then the cells were oxidized in air at 850°C for 6 h to increase the metal support wettability for infiltration and create a continuous oxide scale.

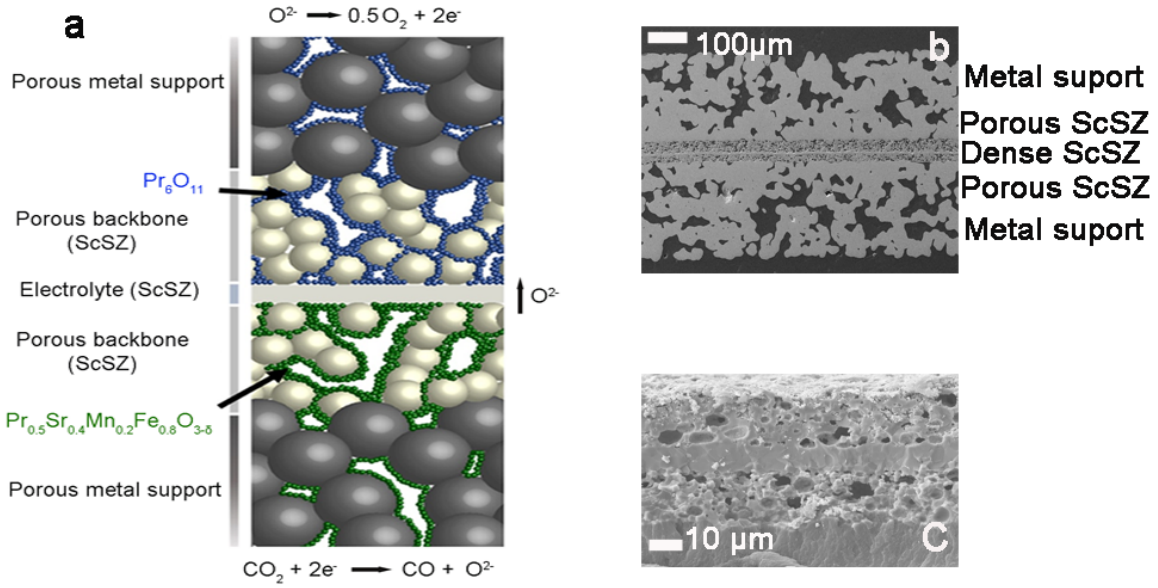

Fig. 1. Cell structure. a: Schematic of the metal supported symmetric cell with PSMF and Pr_6O_{11} catalysts under CO_2 electrolysis operation. Adapted from reference (39) with permission. b: cross-section of a sintered metal support cell, c: cross-section of PSMF-ScSZ‖ScSZ‖Pr_6O_{11}-ScSZ electrode and electrolyte layers.

2.2. PSMF/Pr_6O_{11} Catalyst Infiltration and Co-firing

$Pr_{0.5}Sr_{0.4}Mn_{0.2}Fe_{0.8}O_{3-\delta}$ (PSMF) and Pr_6O_{11} electrocatalysts were deposited in the ScSZ electrode scaffolds by vacuum assisted infiltration and co-firing. This A-site deficient composition was chosen to avoid formation of secondary phases such as Pr-oxides, when fired in air. Mild vacuum removes air from the inner pores of the electrodes and allows nitrate solution to penetrate into the electrode/electrolyte interface. The edge of the cell (1-2 mm) was covered with Acrylic paint (Liquitex) to prevent catalyst deposition on the perimeter area, thereby reducing interference with the glass seal to obtain a good open circuit voltage (OCV). For PSMF, stoichiometric mixtures of Pr, Sr, Mo, and Fe-nitrates (Sigma Aldrich, Pr: Sr: Mo: Fe=5:4:2:8 mmol) were mixed with Triton-X surfactant/water (1.2:10 wt), and citric acid chelating agent (26 mmol, Sigma Aldrich).

The PSMF composition was selected from parallel work on conventional cells with solid-state catalyst synthesis, which will be reported elsewhere. A solution with 0.5 M total nitrates was initially utilized, and 0.15 M solution was later adopted for thinner catalyst deposition. Ammonia solution (Sigma Aldrich, 25%) was added to adjust the pH solution to near 7. The resulting PSMF precursor solution was dripped onto the CO_2 electrode, mild vacuum was applied for ~30 seconds to remove air from the cell, excess surface solution was wiped off, the solution was dried at 90°C for 10 mins, and then the cell was fired in air 850°C for 30 mins to convert the nitrates to PSMF catalyst phase. Then Pr nitrate solution (~1.5 M, ethylene glycol and water as solvents (1:3 weight)) for the oxygen electrode was infiltrated and fired using a similar procedure. Pr-oxide was infiltrated 8 cycles and fired at 800°C to achieve the highest activity, based on earlier work (31). For both electrodes, fast firing was achieved by quickly placing the cells in a pre-heated furnace, a process uniquely enabled by the fast-thermal cycling capability of metal supported cells. Fast firing creates more porosity in electrode catalysts compared to slow firing (40).

2.3. Cell testing

The setup for cell testing is shown in Fig. S1. Metal-supported button cells were mounted onto 410 stainless steel test rigs (41). Pt mesh was spot welded to both sides of the cells and connected with a potentiostat (Biologic VMP3) by Pt wires. Glass powder (GM31107, Schott) mixed with acrylic based binder (Schott AG) was applied as a paste by syringe to the edges of the cells, heated up to 800°C at 2°C min^{-1} and cured for 1 h. The cell temperature was then ramped to the desired operating temperature at 2°C min^{-1}. This sealing procedure was evaluated by testing a separate cell in hydrogen-air, with good sealing confirmed with an OCV of 1.1 V at 750°C (Fig. S2).

The cell and test rig hot zone were enclosed in a 2" diameter closed-end alumina tube, with the bottom open end filled with insulating alumina wool (Zircar). CO_2 gas was fed at 30 to 120 cm^3 min^{-1} with 14% Ar as internal standard for gas chromatography (GC) analysis. The oxygen electrode (PrO_x) was exposed to air flowing at 300 cm^3 min^{-1}. Purified ambient air (using 3 stage Parker Ballston air filter) with <3% H_2O was utilized for this study. Open circuit voltage (OCV), cyclic voltammetry (CV) from OCV to OCV+1.8 V, electrochemical impedance spectroscopy (EIS) and cell performance (IV-PI and I-t) were recorded with a multichannel potentiostat (Biologic VMP3 with 10 A boosters). EIS were measured at the conditions of 10k-0.05 Hz, 12 points per decade, 120 mV amplitude, OCV or OCV+1.2 V. The CO_2 electrode exhaust gas line was connected to a gas chromatograph for product analysis described below.

2.4. Characterization

To prepare samples for XRD analysis (Bruker D2 Phaser) and determine optimum firing temperature, PSMF infiltration solution was dried at 90°C and then fired at 800 to 900°C for 30 min to produce powder. A portion of the PSMF powder fired at 850 °C was reduced at 800°C in 2% H_2/Ar for 10 h. Room-temperature XRD analysis was performed with a scanning speed of 5° min^{-1} at a step size of 0.02°.

Metal supports were peeled apart for both fresh and posttest cells to reveal the thin ceramic electrode layers. XRD of the electrodes was performed. Then Au was sputtered on select samples for scanning electron microscope (SEM) analyses. A Zeiss Gemini Ultra-55 SEM at voltages of 5-20 kV with an energy dispersive X-ray (EDX) detector was utilized to obtain field emission scanning electron microscopy (FESEM) images (5-20 kV) and element maps (20 kV).

An online GC (SRI 8610C) was utilized to analyze the products of the cathode outlet. The inlet and outlet gas lines were heated above 100°C using heating tape. The GC was equipped with a HaySep D column, a TCD detector, and an FID detector with a methanizer. The oven temperature was set at 40°C for 10 mins and then ramped at 20°C/min to 210°C for 6 mins. Certified gas mixtures were used to calibrate the GC (34).

3. Results and Discussion

3.1. PSMF Catalyst Structure, Morphology, and Optimization

The goal of the catalyst synthesis is to obtain pure perovskite PSMF after firing in air, and then reduce PSMF catalysts using *in situ* exsolution process to form RP-PSMF catalysts. Initially, the appropriate temperature for firing the PSMF catalyst was determined. For metal supported SOCs, a maximum catalyst firing temperature of 900°C or lower is preferred to avoid excess oxidation of metal support and maintain high catalyst surface area. Our previous studies of other catalyst compositions (SFM, Pr_6O_{11}, LSCF, SDC, Ni-SDC) indicate that a firing temperature around 800 to 850 °C generally leads to the correct phase formation, high crystallinity, and a good balance between initial performance and long-term durability (31, 33, 34, 36, 37). Therefore, we studied the range 800 to 900 °C for PSMF, and utilized XRD to check phase purity and catalyst structure for selection of the proper firing and reducing temperature. A minor second phase (SrO) is present after firing at 800°C for 30 min, Fig 2a. Pure PSMF phase was achieved at 850°C and 900°C, a considerably lower temperature than the 1100°C firing used previously for sol–gel process (11). In full cells, to minimize stainless steel oxidation and further crystallize PSMF and keep it firmly attached to the ScSZ support, an extending firing time of 2h at 850 °C was selected. After reducing in 2% H_2/Ar (balance) at 800°C for 10 h, the perovskite PSMF was transformed to

the tetragonal RP-PSMF with additional small peaks corresponding to metallic iron (Fe, Fig. 3a, b) and praseodymium oxide (Pr_2O_3) phases, Fig. 2b. The XRD pattern is nearly identical to that reported previously for *in situ* exsolved PSMF catalyst (11). A similar transformation is expected to occur during cell operation, as the catalyst is reduced by CO generated electrochemically. Due to the high surface area, small particle size, and relatively low loading of infiltrated catalysts, conversion between the oxidized and reduced forms occurs within seconds at the operating temperature (40).

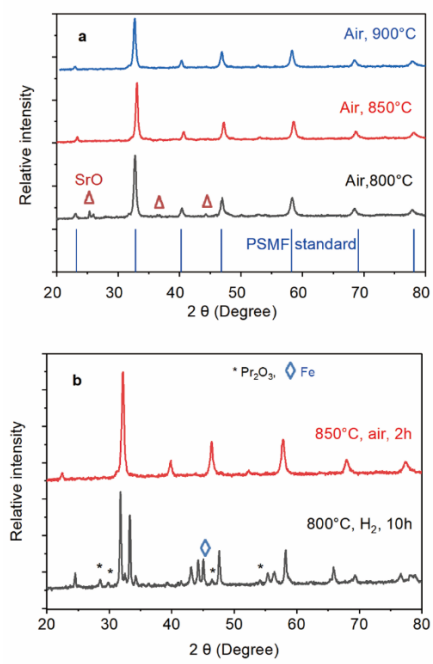

Fig. 2. PSMF phase purity and structure determined by XRD. a: PSMF powder obtained from drying infiltration solution at 90°C, and firing at 800 to 900°C in air for 30 min. b: PSMF fired in air at 850°C for 2 h, and after further firing in 2% hydrogen-Ar (balance) at 800°C.

Further optimization of PSMF catalyst infiltration focused on coating thickness and porosity. The optimal number of infiltration cycles was determined by testing cells with 2 to 5 cycles of PSMF infiltration (Fig. S3). Cells with 3x PSMF infiltration obtained the best cell performance as

determined by EIS and VI curves. The concentration of the PSMF precursor solution significantly impacted the catalyst coating structure. Whereas the standard 0.5 M solution produced a ~1.5 μm thick, dense coating of large PSMF particles (Fig. 3c), a diluted 0.15 M precursor solution enabled a ~0.2 μm thick, uniform, and porous PSMF catalyst coating with finer particles (Fig. 3d). These are referred to as "thick" and "thin" PSMF catalysts, respectively.

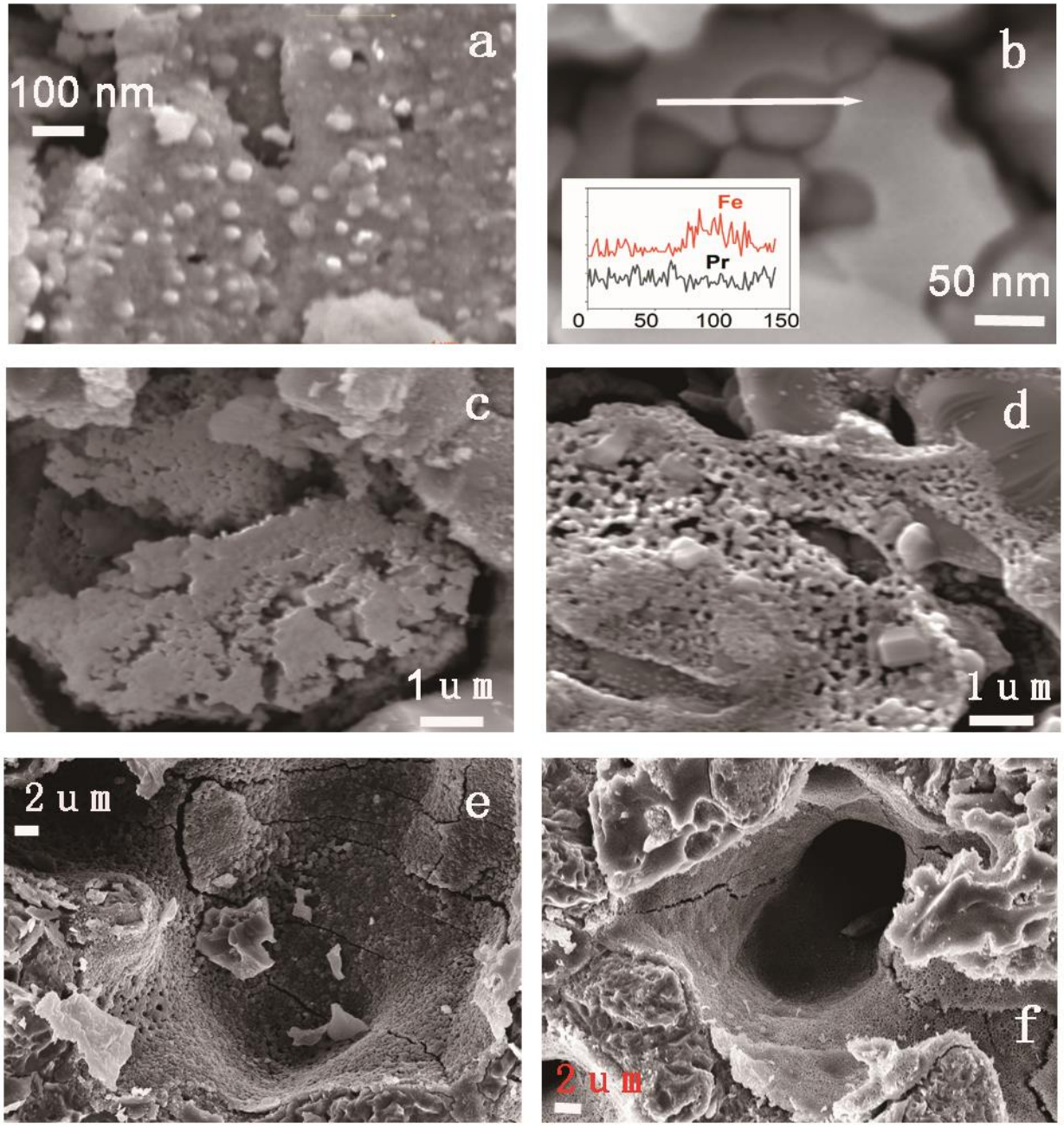

Fig. 3. **Morphology of PSMF/Pr_6O_{11} catalyst.** a,b: exsolved Fe particles on PSMF catalyst after firing at 850°C in air (2h) and reduced in 2% H_2/Ar (balance) for 10 h (inset: line-scan EDX of Fe and Pr at the arrow position, full spectra were shown in Fig. S4). Thick PSMF catalyst particles deposited from 0.5M solution in the (c) ScSZ electrode pores and (e) in the metal support pores. Thin PSMF catalyst particles deposited from 0.15 M solution in (d) the ScSZ electrode pores. (f) Pr_6O_{11} infiltrated in the metal support pores

The thin PSMF catalyst provides better performance, as shown in Fig. 4. For thick PSMF, the current densities at 1.5 V are 0.026, 0.054, 0.10, 0.19, and 0.16 A cm^{-2} for operating temperatures of 600, 650, 700, 750, and 800°C, respectively. Rohm and Rp at 750°C are 0.55, and 4.2 Ω cm^2, respectively (Fig. 4, a and b). The cell performance was limited by Rp due to thickness and density of the PSMF layer which limits TPB area for the catalytic sites. The optimal temperature is around 750°C for the thick PSMF cell. For thin PSMF, a smaller operating temperature range of 700 to 800°C was selected. The current densities at 1.5 V are 0.40, 0.62, 0.86, 0.79, and 0.77 A cm^{-2} for operating temperatures of 700, 725, 750, 775, and 800°C, respectively. Rohm and Rp at 750°C are 0.44 and 1.23 Ω cm^2, respectively (Fig. 4, c and d). In Fig. 4b, the electrode impedance at 800°C is lower than that at 750°C with thick PSMF, while the electrode impedances at 750°C and 800°C are similar for thin PSMF. Current density may be higher at 800°C, however 750°C is considered an upper limit for metal support long term operation due to thermal activation of the stainless steel oxidation (32). Other degradation mechanisms such as catalyst coarsening and Cr migration are also thermally activated. Based on these results and considerations, 750°C was chosen for further testing below. DRT analysis suggests that increasing temperature above 750°C increases impedance of the oxygen ion transfer processes (Fig. S5), which may be due to increased catalyst

coarsening and chromium evaporation (31, 37). This optimized cell performance (0.86 A cm^{-2} at 1.5V and 750°C) compares favorably with previous CO_2 reduction cells based on zirconia-electrolyte-supported designs with catalysts prepared by solid state synthesis, for example, Ag-GDC‖YSZ‖LSM (0.68 A cm^{-2} at 800°C) (42) and LSFN‖GDC-YSZ-GDC‖LSFN (0.65 A cm^{-2} at 800°C) (16). Performance of a cell with PSMF catalyst was higher (PSMF-GDC‖LSGM‖LSCF-GDC, 1.61 A cm^{-2} at 750°C), presumably due to the use of LSGM electrolyte and composite electrodes (11).

Table 1. Comparison of SOC performance at operating temperature of 750-800°C

Electrolyte	Fuel electrode	Oxygen electrode	Temperature (°C)	Effective area (cm^2)	I at 1.5 V ($A.cm^2$)	Ref.
LSGM, 190 µm	RP-PSMF	LSCF-GDC	750	~1.	1.61	(11)
LSGM/LDC, 230 µm	SFM-SDC	LSCF-SDC	750	~1	0.49	(20)
ScSZ, 12 µm	RP-PSMF	Pr_6O_{11}	750 800	~4	0.86 0.77	This work
GDC-YSZ-GDC, 420 µm	LSFN	LSFN	800	~1	0.65	(16)
YSZ, 130 µm	Ag-GDC	LSM	800	2	0.68	(42)

Note: GDC: $Ga_{0.2}Ce_{0.8}O_{2-\delta}$, SDC: $Sm_{0.2}Ce_{0.8}O_{2-\delta}$, ScSZ: $Sc_{0.1}Ce_{0.01}Zr_{0.89}O_{2-\delta}$, LSCF: $(La_{0.6}Sr_{0.4})_{0.95}Co_{0.2}Fe_{0.8}O_{3-\delta}$, YSZ: $Y_{0.08}Zr_{0.92}O_{2-\delta}$, LSFN: $La_{0.6}Sr_{0.4}Fe_{0.8}Ni_{0.2}O_{3-\delta}$, LSM: $(La_{0.8}Sr_{0.2})_{0.95}MnO_{3-\delta}$

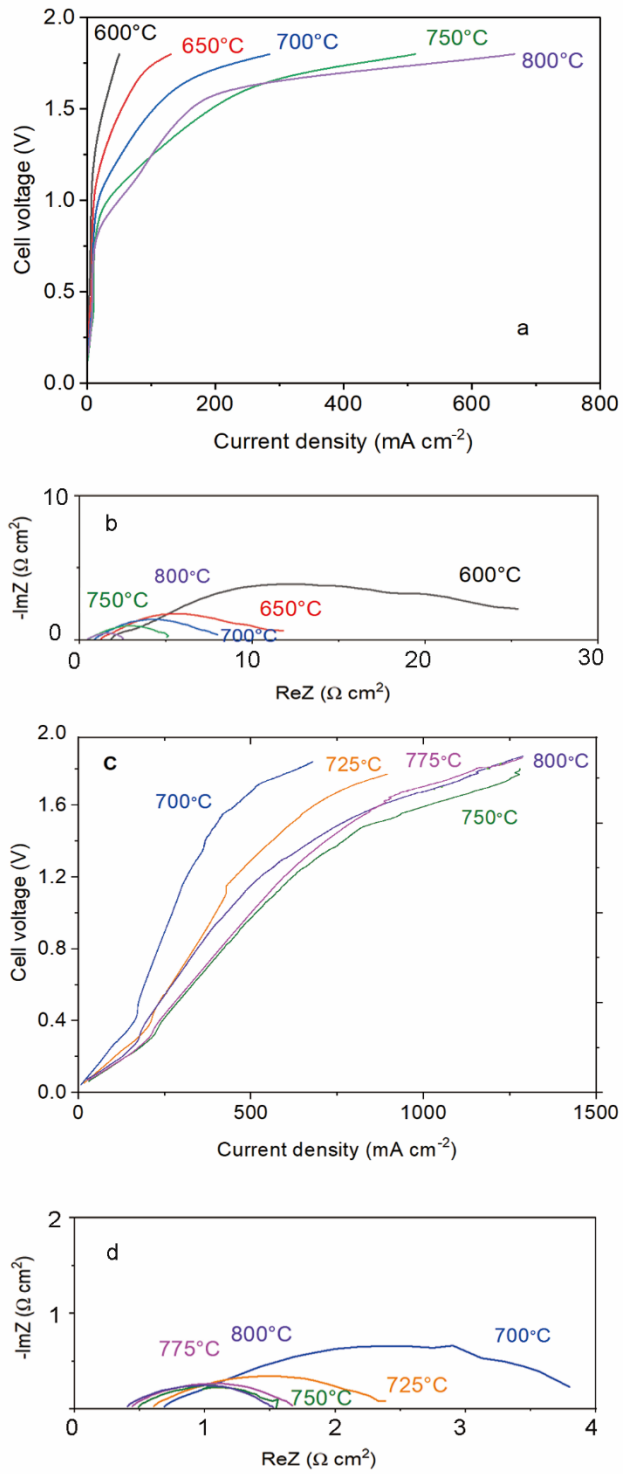

Fig. 4. Electrochemical characterization of the metal supported PSMF‖SSZ‖Pr_6O_{11} cells in CO_2/air at an operating temperature range of 600-800°C. a, c: VI curves and b, d: EIS spectra of a, b: thick PSMF cells and c, d: thin PSMF cells.

3.2. Impact of operation conditions on CO_2 conversion

Cells with thin PSMF catalyst were operated over a range of temperatures and voltages, with GC analysis of the exhaust gas used to determine CO_2 conversion, Fig. 5. The performance is quite sensitive to both operating variables. At constant cell voltage of 1.5 V, CO_2 conversion (38.4%) and current density (0.86 A cm^{-2}) are maximized at 750°C, as discussed above in Section 3.1. This temperature is at the upper end of the acceptable range for metal-supported cells, considering the oxidation of metal support (32). The impact of operating potential was determined at 750°C, using another similar cell, Fig. 5b. Above 0.4 V, the CO_2 conversion increases dramatically with overpotential, reaching 57.2% at 1.8 V. The CO_2 conversion and current density follow identical trends, consistent with 92.3%±4.5% Faradaic efficiency calculated for the electrochemical reaction.

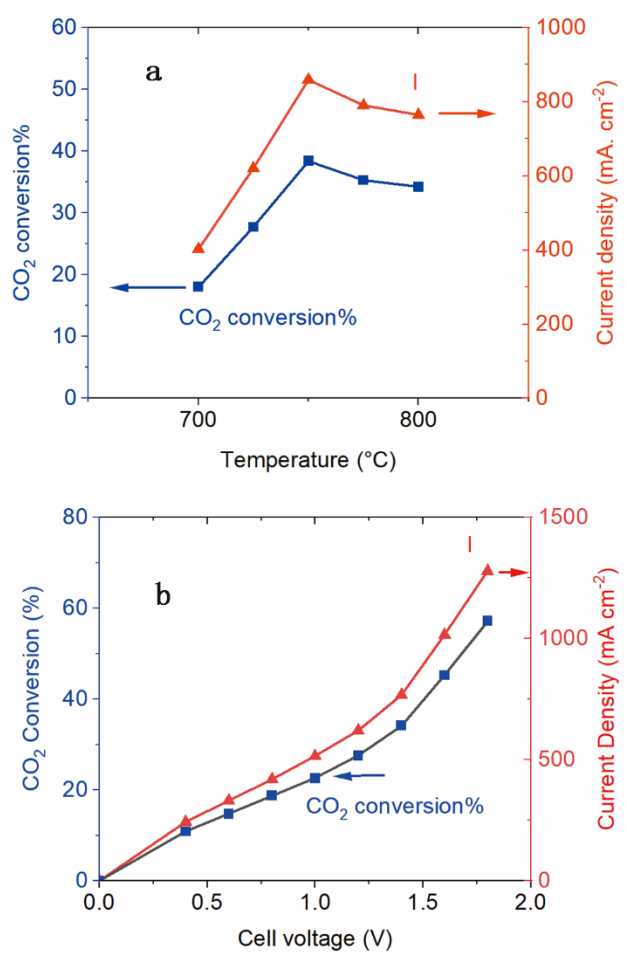

Fig. 5. Impact of operating temperature and overpotential. A PSMF‖SSZ‖Pr_6O_{11} cell with thin PSMF operated in CO_2/air over a range of a: temperature (at 1.5 V) and b: cell voltage (at 750°C).

3.3. Cell stability

Multiple MS-SOCs with PSMF cathode and Pr_6O_{11} anode maintained good stability during 150+ h CO_2 electrolysis operation at 750°C (Fig. 6 and Fig. S6). This cell was activated for about 24 h (not shown) and therefore an initial increase of I was not shown, in contrast to Fig. S6. Operating at constant voltage (this study) or constant current (11) continuously produces CO, maintaining the RP-PSMF catalyst phase without the need for protective CO-containing feed gas,

in contrast to another report (43). A cell with thin PSMF showed relatively stable performance with a moderate initial current density of 535 mA cm^{-2} at 1.2 V. The current density remained almost constant for 150 h. The CO_2 conversion dropped slightly from 22.6% at 50 h to 20.6% at 110 h, and then remained stable at 20.2% throughout the rest of the testing period. The average degradation rate of CO_2 conversion was 6.6%/100h while current density was stable. We believe this is due to slight degradation of the seal, leading to reduced CO_2 Faradaic efficiency.

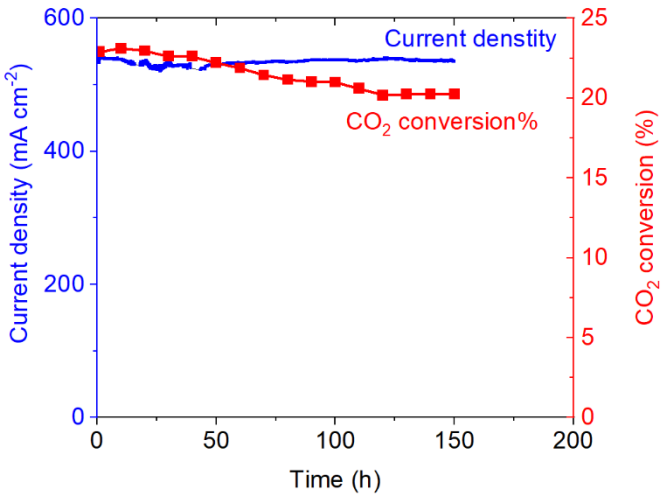

Fig. 6. Cell stability. Potentiostatic operation of a metal-supported PSMF‖SSZ‖Pr_6O_{11} at 750°C and cell voltage of 1.2 V with 60 cm^3 min^{-1} CO_2-10 cm^3 min^{-1} Ar, and 300 cm^3 min^{-1} air.

3.4. Post-operation Characterization and Cell Activation/Degradation

After CO_2 electrolysis tests, the cells were cooled down in hydrogen. One metal support was peeled off, exposing part of the PSMF and Pr_6O_{11} electrodes for SEM-EDS characterization. Fig. 7 shows the morphologies of PSMF catalysts and Pr_6O_{11} catalyst. Few exsolved particles were formed at thick PSMF catalyst surface (Fig. 7a). Large amounts of nanoparticles (≤50 nm) were observed in thin and porous PSMF catalysts after the 150 h test (Fig 7b). These particles are consistent with the exsolved Fe observed in Fig. 3b. Park et al. revealed that these exsolved

nanoparticles are Fe particles by SEM-EDS and XPS and these iron nanoparticles were incorporated into the lattice after oxidation at high temperature (11). Reduction of mixed valent metal ions (Fe^{3+}/Fe^{2+}, Mn^{4+}/Mn^{3+}) promotes formation of oxygen vacancies during the *in situ* exsolution processes (Equations 1, 2):

$$2Fe^{3+} + O_o^x + H_2 \rightarrow 2Fe^{2+} + H_2O + V_o^{\cdot\cdot} \qquad (1)$$

$$2Fe^{3+} + O_o^x + CO \rightarrow 2Fe^{2+} + CO_2 + V_o^{\cdot\cdot} \qquad (2)$$

Formation of oxygen vacancies promotes the adsorption of CO_2 (44) and accelerates initial electrochemical reactions (Figs. S5, a and b). *In situ* exsolution proceeds more easily and completely in thin and porous PSMF catalysts, yielding improved performance as discussed above (Figs. 4 a and c). The porous Pr_6O_{11} catalyst on ScSZ support has no apparent aggregation observed, similar to our previous study of oxidative coupling of methane (37) (Fig. 7c, d).

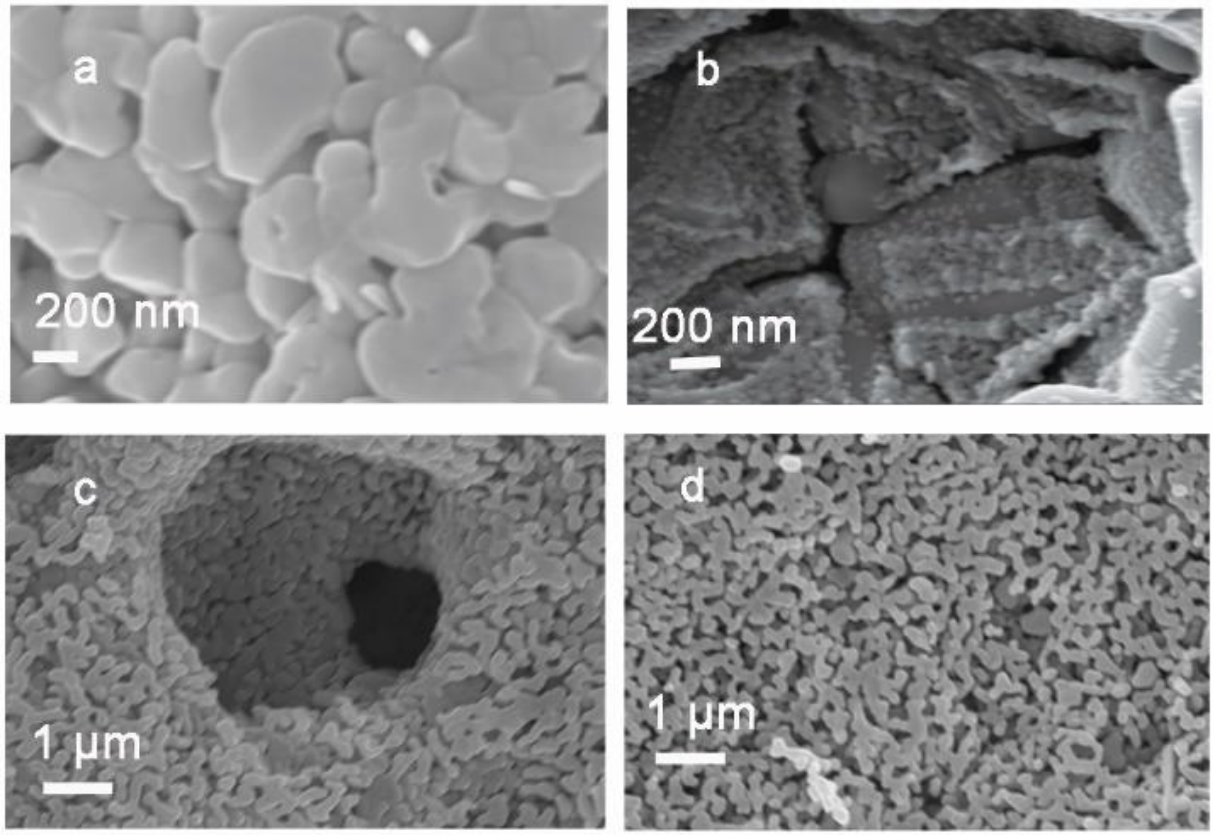

Fig. 7. Pretest and posttest PSMF and Pr_6O_{11} catalyst. a: posttest thick PSMF catalyst, b: 150 h posttest thin PSMF catalyst, c; pretest Pr_6O_{11}, d: posttest Pr_6O_{11}.

After the CO_2 electrolysis tests, chromium deposition was evaluated by EDS analysis of the cross-section (Fig. S7). Cr in Pr_6O_{11} was about 1.8 wt%. Cr_2O_3 layer was formed during pre-oxidation and CO_2 electrolysis as observed in our previous reports (37). For long term operation (>1kh), electrophoretic protective coatings are being developed and will be added to the metal support to suppress Cr_2O_3 formation and mitigate Cr evaporation (32).

No carbon was observed in the posttest PSMF catalysts by Raman spectroscopy (Fig. S8). A wide peak at 1350 cm^{-1} was observed in the spectrum of the fresh PSMF catalyst, which was assigned to doped $SrFeO_3$ (44). This peak overlaps with D band of amorphous carbon. However, the intensity of this peak was not increased after operation. Moreover, no carbon G band at 1580 cm^{-1} was observed, suggesting the absence of carbon.

4. Conclusions

MS-SOCs with infiltrated PSMF cathode catalyst and Pr_6O_{11} anode catalyst have been developed for CO_2 electrolysis. The number of catalyst infiltration cycles, catalyst precursor solution concentration, and firing/reducing temperatures were optimized to increase cell performance. The catalyst structure-performance relationship has been revealed by electrochemical characterization, SEM, and GC measurements. The current density and CO_2 conversion are highest at 750°C, with current densities of 0.54 A cm^{-2} and 0.86 A cm^{-2} achieved at 1.2V and 1.5 V, respectively. The highest CO_2 conversion reached 57.2% at 750°C and 1.8 V using thin PSMF catalyst. Thin and porous RP-PSMF phase formation was observed in SEM

images of the posttest PSMF cathode. The cell showed good durability during potentiostatic operation for 150 h, with stable current density and minor decrease of CO_2 conversion.

Acknowledgements

This work was funded in part by the U.S. Department of Energy under contract no. DE-AC02-05CH11231. This work was funded in part by the U.S. Department of Energy, Office of Energy Efficiency and Renewable Energy, Industrial Efficiency and Decarbonization Office (IEDO), U.S. Department of Energy under contract number DE-AC02-05CH11231. Work at the Molecular Foundry was supported by the Office of Science, Office of Basic Energy Sciences, of the U.S. Department of Energy under Contract No. DE-AC02-05CH11231. This document was prepared as an account of work sponsored by the United States Government. While this document is believed to contain correct information, neither the United States Government nor any agency thereof, nor the Regents of the University of California, nor any of their employees, makes any warranty, express or implied, or assumes any legal responsibility for the accuracy, completeness, or usefulness of any information, apparatus, product, or process disclosed, or represents that its use would not infringe privately owned rights. Reference herein to any specific commercial product, process, or service by its trade name, trademark, manufacturer, or otherwise, does not necessarily constitute or imply its endorsement, recommendation, or favoring by the United States Government or any agency thereof, or the Regents of the University of California. The views and opinions of authors expressed herein do not necessarily state or reflect those of the United States Government or any agency thereof or the Regents of the University of California. This manuscript has been authored by an author at Lawrence Berkeley National Laboratory under Contract No.

DE-AC02-05CH11231 with the U.S. Department of Energy. The U.S. Government retains, and the publisher, by accepting the article for publication, acknowledges, that the U.S. Government retains a non-exclusive, paid-up, irrevocable, world-wide license to publish or reproduce the published form of this manuscript, or allow others to do so, for U.S. Government purposes.

References

1. Y. Song, X. Zhang, K. Xie, G. Wang and X. Bao, *Adv Mater*, **31**, 1902033 (2019).
2. J. A. Hoffman, M. H. Hecht, D. Rapp, J. J. Hartvigsen, J. G. SooHoo, A. M. Aboobaker, J. B. McClean, A. M. Liu, E. D. Hinterman, M. Nasr, S. Hariharan, K. J. Horn, F. E. Meyen, H. Okkels, P. Steen, S. Elangovan, C. Graves, P. Khopkar, M. B. Madsen, G. E. Voecks, P. H. Smith, T. L. Skafte, K. R. Araghi and D. J. Eisenman, *Sci. Adv.*, **8**, 8636 (2022).
3. C. Zhu, S. Hou, X. Hu, J. Lu, F. Chen and K. Xie, *Nat Commun*, **10**, 1173 (2019).
4. Z. Yan, J. L. Hitt, J. A. Turner and T. E. Mallouk, *Proc Natl Acad Sci U S A*, **117**, 12558 (2020).
5. B. Hu, C. Guild and S. L. Suib, *J. CO_2 Util.*, **1**, 18 (2013).
6. B. Hu, S. Frueh, H. F. Garces, L. Zhang, M. Aindow, C. Brooks, E. Kreidler and S. L. Suib, *Appl. Catal. B*, **132-133**, 54 (2013).
7. S. van Bavel, S. Verma, E. Negro and M. Bracht, *ACS Energy Letters*, **5**, 2597 (2020).
8. L. Wang, M. Chen, R. Küngas, T.-E. Lin, S. Diethelm, F. Maréchal and J. Van herle, *Renew. Sustain. Energy Rev.*, **110**, 174 (2019).
9. R. Küngas, *J. Electrochem.Soc.*, **167** (2020).
10. F. Thaler, Q. Fang, U. de Haart, L. G. J. de Haart, R. Peters and L. Blum, *ECS Trans.*, **103**, 636 (2021).

11. K.-Y. Park, T. Lee, W. Wang, H. Lia and F. Chen, *J. Mater. Chem A*, **11**, 21354 (2023).

12. Y. Zhou, L. Lin, Y. Song, X. Zhang, H. Lv, Q. Liu, Z. Zhou, N. Ta, G. Wang and X. Bao, *Nano Energy*, **71** (2020).

13. T. L. Skafte, C. Graves, P. Blennow and J. Hjelm, *ECS Trans.*, **68**, 3429 (2015).

14. A. K. Clausen, M. L. Traulsen, P. V. Hendriksen, X. Sun and A. Hauch, *ECS Trans.*, **103**, 1945 (2021).

15. C. Cui, Y. Wang, Y. Tong, Z. Zhan, C. Chen and S. Wang, *J. Electrochem. Soc.*, **168** (2021).

16. Y. Tian, H. Zheng, L. Zhang, B. Chi, J. Pu and J. Li, *J. Electrochem. Soc.*, **165**, 17 (2018).

17. X. Yue and J. T. S. Irvine, *J. Electrochem. Soc.*, **159**, F442 (2012).

18. L. L. Lu, C. Ni, M. Cassidy and J. T. S. Irvine, *J. Mater. Chem. A*, **4**, 11708 (2016).

19. M. Yin, Z. Wang, C. Yang, J. Pu and B. Chi, *J. Electrochem. Soc.*, **170**, 034501 (2023).

20. Y. Li, X. Chen, Y. Yang, Y. Jiang and C. Xia, *ACS Sustain. Chem. Eng.*, **5**, 11403 (2017).

21. Y. Wang, T. Liu, S. Fang and F. Chen, *J. Power Sources*, **305**, 240 (2016).

22. D. Neagu, T. Oh, D. Miller, H. Ménard, S. M. Bukhari, S. R. Gamble, R. J. Gorte, J. M. Vohs and J. T. S. Irvine, *Nat Commun* **6**, 8120 (2015).

23. H. Lv, L. Lin, X. Zhang, Y. Song, H. Matsumoto, C. Zeng, N. Ta, W. Liu, D. Gao, G. Wang and X. Bao, *Adv Mater*, **32**, 1906193 (2020).

24. Y. Yang, Y. Wang, Z. Yang, Y. Chen and S. Peng, *J. Power Sources*, **478** (2020).

25. J. T. S. Irvine and K. Xie, *ECS Trans.*, **91**, 2565 (2019).

26. C. Ni, J. Zhou, Z. Zhang, S. Li, J. Ni, K. Wu and J. T. S. Irvine, *Energy Environ. Sci.*, **14**, 6287 (2021).

27. M. C. Tucker, *J. Power Sources*, **395**, 314 (2018).

28. M. C. Tucker and A. S. Ying, *Int. J. Hydrogen Energy*, **42**, 24426 (2017).

29. M. C. Tucker, *J. Power Sources*, **369**, 6 (2017).

30. Z. Zhu, B. Hu and M. C. Tucker, *Int. J. Hydrogen Energy*, **59**, 316 (2024).

31. B. Hu, G. Lau, D. Song, Y. Fukuyama and M. C. Tucker, *J. Power Sources*, **555** (2023).

32. F. Shen, M. M. Welander and M. C. Tucker, *Int. J. Hydrogen Energy*, **48**, 12168 (2023).

33. M. M. Welander, B. Hu and M. C. Tucker, *Inter. J. Hydrogen Energy*, **47**, 11261 (2022).

34. B. Hu, G. Lau, K. X. Lee, S. Belko, P. Singh and M. C. Tucker, *J. Power Sources*, **582** (2023).

35. E. Dogdibegovic, Y. Fukuyama and M. C. Tucker, *J. Power Sources*, **449** (2020).

36. M. M. Welander, B. Hu and M. C. Tucker, *Int. J. Hydrogen Energy*, **48**, 21578 (2023).

37. B. Hu, F. Rosner, H. Breunig, A. Sarycheva, R. Kostecki and M. C. Tucker, *Int. J. Hydrogen Energy*, **48**, 33537 (2023).

38. E. Dogdibegovic, R. Wang, G. Y. Lau and M. C. Tucker, *J. Power Sources*, **410-411**, 91 (2019).

39. Wang R, Dogdibegovic E, Lau GY and T. MC., *Energy Technol* **7**, 1801154 (2019).

40. E. Dogdibegovic, Y. Cheng, F. Shen, R. Wang, B. Hu and M. C. Tucker, *J. Power Sources*, **489** (2021).

41. F. Shen, M. M. Welander and M. C. Tucker, *Front Energ. Res.*, **10** (2022).

42. Y. Xie, J. Xiao, D. Liu, J. Liu and C. Yang, *J. Electrochem. Soc.*, **162**, F397 (2015).

43. S. Lee, M. Kim, K. T. Lee, J. T. S. Irvine and T. H. Shin, *Adv. Energy Mater.*, **11** (2021).

44. A. K. Opitz, A. Nenning, C. Rameshan, M. Kubicek, T. Gotsch, R. Blume, M. Havecker, A. Knop-Gericke, G. Rupprechter, B. Klotzer and J. Fleig, *ACS Appl Mater Interfaces*, **9**, 35847 (2017).